2022-02-01

OrthoSpar, a novel substructure concept for floating offshore wind turbines: Physical model tests under towing conditions

Buttner, T

10.1016/j.oceaneng.2021.110508
Ocean Engineering
Elsevier BV

OrthoSpar, a novel substructure concept for floating offshore wind turbines: Physical model tests under towing conditions

T. Büttner[A], C. Pérez-Collazo[B*], J Abanades[C], M. Hann[D], P. Harper[E], D. Greaves[C], Stiesdal, H.[F]

[A] SeaRenergy Offshore Holding GmbH & Cie., Hamburg, Germany.

[B] Defense University Centre at the Spanish Naval Academy, Plaza de España, s/n, 36920 Marín, Spain.

[C] TYPSA, Parque empresarial Táctica, Paterna, Valencia, Spain.

[D] School of Engineering Computing and Mathematics, University of Plymouth, Reynolds Building, Plymouth, UK.

[E] Faculty of Engineering, University of Bristol, University Walk, Bristol, UK.

[F] Stiesdal Offshore Technologies A/S, Odense C, Denmark

[*] Corresponding author, email: carlos.perez.collazo@cud.uvigo.es; ORCID: 0000-0002-9191-6959

ABSTRACT

An important condition of any port-assembled floating offshore wind turbine concept is the de-ballasted transport stage. As the hydrostatic and dynamic stability may vary greatly from the operational condition, it needs to be carefully investigated in early stages of the design-phase. In this work, physical modelling of the transport of the de-ballasted OrthoSpar device was carried out to determine roll and pitch RAOs, as well as load characteristics of the towing line. Towing was simulated with a stationary model being subjected to currents. To examine the influence of wave direction, a range of model orientations towards the incident waves were tested in still water and together with the simulated towing state. Roll and pitch motions were found to be highly dependent on the wave frequency and a result of a low damping ratio. The towing load amplitude was found to be influenced by the towing direction regarding the wave direction.

Keywords: Floating Offshore Wind Turbine, OrthoSpar, Towing, Tank tests, Motion response, RAO

Acronyms: FOWT, Floating offshore wind turbine; LCOE, Levelised cost of energy; RAO, Response amplitude operator; NRMSE, Normalises root mean squared error.

1. INTRODUCTION

Renewable energies will play an increasing role in the future energy supply. The EU targets a share of 40% energy from renewable resources by 2030 to reduce greenhouse gas emissions and fight climate change (European Commission, 2021). This means the EU will need boost 2.5 times todays wind power installed capacity from 180 GW to 450 GW (Wind Europe, 2021). Despite providing energy at a lower cost, onshore wind energy installation rates show much less growth compared to offshore wind in the EU (Fraile and Tardieu, 2018). In this line the EU strategy on offshore renewable energy foresees 60 GW of installed capacity by 2030 and 300 GW by 2050 (European Commission, 2020).

The majority of offshore wind turbines are fixed structures, taking advantage of the lower cost of installation on shallow and intermediate water depths (James and Costa Ros, 2015) –i.e., on 2020 floating foundations only represented the 0.2% of the total installed turbines in the EU (Ramírez et al., 2021). In order to achieve the foreseen installation targets by 2050 a move towards the vast deep water grounds –i.e., those with water depths larger than 60 m– is required. Therefore, floating offshore wind turbines (FOWTs) are called to make this technology available for most coastal areas worldwide (Castro-Santos et al., 2020; Castro-Santos and Diaz-Casas, 2015). Moving towards deeper grounds will also contribute to increase offshore wind capacity factor (Schuldt, 2006).

Research on FOWTs has mainly been carried out during the last decade and its was driven by the successful deployment of two full-scale concepts, HyWind from Statoil in 2009 in Norway ("Equinor," 2019) and WindFloat from Principle Power in 2011 out of the coast of Portugal (Principle Power Inc, 2015). Although, in recent years there have been relevant advancements in the development of FOWTs, the technology is still at an early stage and plenty of different concepts exist, as it can be seen in (James and Costa Ros, 2015) and in (Tande et al., 2015). One of the key challenges faced by FOWTs is to drive down its levelised costs of energy (LCOE) to make it competitive with fixed offshore wind, and in ultimate instance with onshore wind. The costs of assembling a FOWT offshore is three to four

times higher than the onshore assembly of the complete turbine (Myhr et al., 2014), as result of current designs being based on existing concepts from the oil and gas industry. To face this challenge, in recent years, some innovative concepts for FOWTs have been proposed, such as: ("Saitec," 2019) and ("X1 Wind," 2019). What all these new concepts have in common is their ability to be fully assembled at port, then towed to their final production site by means of cheap and widely available offshore tug boats, instead requiring very expensive special-purpose vessels (Butterfield et al., 2005). Therefore, understanding the behaviour of FOWTs while being towed at sea is of particular relevance when comes to design and plan its installation.

In contrast to floating oil and gas structures, FOWT will be installed in greater numbers, calling for increased installation windows to reduce the costs. In turn, this means higher stability requirements to be able to operate in a wider range of sea conditions, not only during the installation process but also in the thereafter operation in the long term –i.e., as metocean conditions of an offshore site have a significant influence on the design, cost and performance of FOWTs (Lerch et al., 2018; Mueller et al., 2015). Existing standards are related to offshore structures in general and consider rough guidelines for the calculation of hydrostatic stability. However, the towing stage of the installation process is not covered individually in sufficient detail (Bureau veritas, 2015; DNV GL, 2018a). The lack of rules for the hydrostatic stability of FOWT structures during pre-installation stages has led to Collu, et al. (2014) to propose guidelines regarding stability during these stages to apply during the conceptual design phase. Furthermore, Roddier, et al. (2010) who tested the WindFloat design in a wave tank have also highlighted the lack of rules for stability calculations during towing conditions of FOWTs.

The EU funded project LIFES50+ (LIFES50+, 2021) analysed the installation of a floating wind farm in the west side of the Scottish Barra Island. The current speeds simulated for the towing (3 kn) can be associated to the service and ultimate limit states in the area. For this location, the design wave height, associated with a return period of 50 years is 15.6 m, with a peak period associated between 12 and 18 s. To complete the metocean conditions, the wind speed in the area at a hub height of 150 m

(typical height for the new generation of wind turbines, + 10 MW) is greater than 12 m/s. This reflects the abundant resource in the area, but also the harsh conditions that suppose a challenge in the design of the components of the wind farm.

The compact semi-submersible concept of the Fukushima Forward project was tested in still water towing conditions to estimate the drag coefficient (Ding et al., 2017). Later, Ishihara and Zhang, (2019) numerically modelled the dynamic multi-body system of a submerged TLP and a tugboat, showing that the foundation was stable in irregular waves with a significant height of 5 m. A 1:37 scale model of the Gicon-TLP concept was tested under operational and towing conditions by (Hyland et al., 2014). Where towing conditions were simulated by pulling the model through the basin against waves at relatively high full-scale speeds (3.54 kn to 7.1 kn), finding an increased towing resistance for the parallel towing configuration, especially in large waves. Adam, et al. (2016) tested in a towing tank a 1:25 scale version of the Gicon-TLP concept with only four buoyancy tanks to analyse the accelerations at the transition piece between the turbine and the platform and the required tug power. As part of the development of a semi-submersible barge to transport TLP structures, Amante, et al. (2016) carried out model tests of the barge while towing the turbine in a towing tank. Additionally, the model was tested in installation configuration in varying orientations to the waves. Finally, Villaespesa, et al. (2018) tested a 1:60 model of the TetraSpar concept with a counterweight during towing in still water to evaluate the towing load. Towing was simulated with a stationary model subjected to a steady current. The four tested configurations included two different device orientations and the options of towing the counterweight among the tanks and behind the model. Based on the results, the configurations of towing the counterweight behind the model showed the lower towing load.

This research deals with the development of the OrthoSpar FOWT, a novel concept investigated first by (Barnes et al., 2017). In particular, the main aim of this paper is to provide experimental data on the stability of a fully assembled wind turbine during towing and installation operations, a topic

where few research has been conducted yet. Hence, this paper addresses the investigation of three of the critical aspects to consider when deploying a FOWT. First, the seakeeping analysis of the platform under different wave conditions –i.e., wave height, period and direction–, to determine the natural frequency of its motion modes. Second, the analysis of the platform's stability when being towed under the effect of waves. Finally, the effect that the different wave conditions would have on the towing loads characteristics was also investigated. To materialise this research, an intensive physical modelling test campaign was carried out using a 1:50 scale model of the OrthoSpar FOWT. For the test campaign, the conditions of interest were the towing and parked (no towing) states in long crested regular waves with relatively long wave periods -i.e., which are characteristic of an ocean swell.

The content of this paper is structured as follows: Section 2 defines the OrthoSpar FOWT concept. Section 3 describes the materials and methods considered for the experimental campaign, including: the physical model, the experimental set-up and testing programme, and the data analysis. The results are presented in Section 4 and discussed in Section 5. Finally, Section 6 draws the conclusions of this work.

2. THE ORTHOSPAR

The OrthoSpar FOWT concept (Figure 1 a) considered for this work, was first developed by (Barnes et al., 2017), on the basis of Hendrik Stiesdals' TetraSpar one (Figure 1 b), whose full-scale demonstrator has been recently deployed out of the south coast of Norway (Borg et al., 2020). Both foundation concepts rely on the design philosophy of maximining the use of components that are highly industrialized and suitable of mass production, with the already existing supply chain -i.e., philosophy this, which would allow important cost reductions in the LCOE by introducing standardising designs and scale economies due to mass production of components.

Both OrthoSpar and TetraSpar use a number of steel slender piles which are connected in an orthogonal or tetrahedral shape, respectively. The floating foundation is moored to the seabed by means of tree catenary mooring lines and the floater it is also connected to a hanged counterweight by

means of tension tendons. Counterweight whose purpose is to increase the overall platform's stability –i.e., combining the advantage of the large surface area of a semi-submersible platform with the high stability of a spar foundation, while keeping a reduce steel mass. OrthoSpar reconsidered the configuration of both the floating foundation and the counterweight to even increase LCOE savings. In order to do this OrthoSpar considered using only 6 steel slender piles instead of the 10 used by TetraSpar. This results on a floating foundation where the wind turbine is now positioned at one of the sides of the platform – i.e., reducing so the stability of the platform. Furthermore, the counterweight has now a more compact star configuration rather than the delta one used by the TetraSpar. Solution this which allows reducing the number of tension tendons. Finally, OrthoSpar also uses small ballast tanks which are connected to each one the lower vertices of the floating platform – note that previous versions of TetraSpar used to have these ballast tanks also, however, during its design optimisation phase these were replaced with some lager diameter lower steel piles (Bredmose et al., 2017; Thomsen et al., 2021).

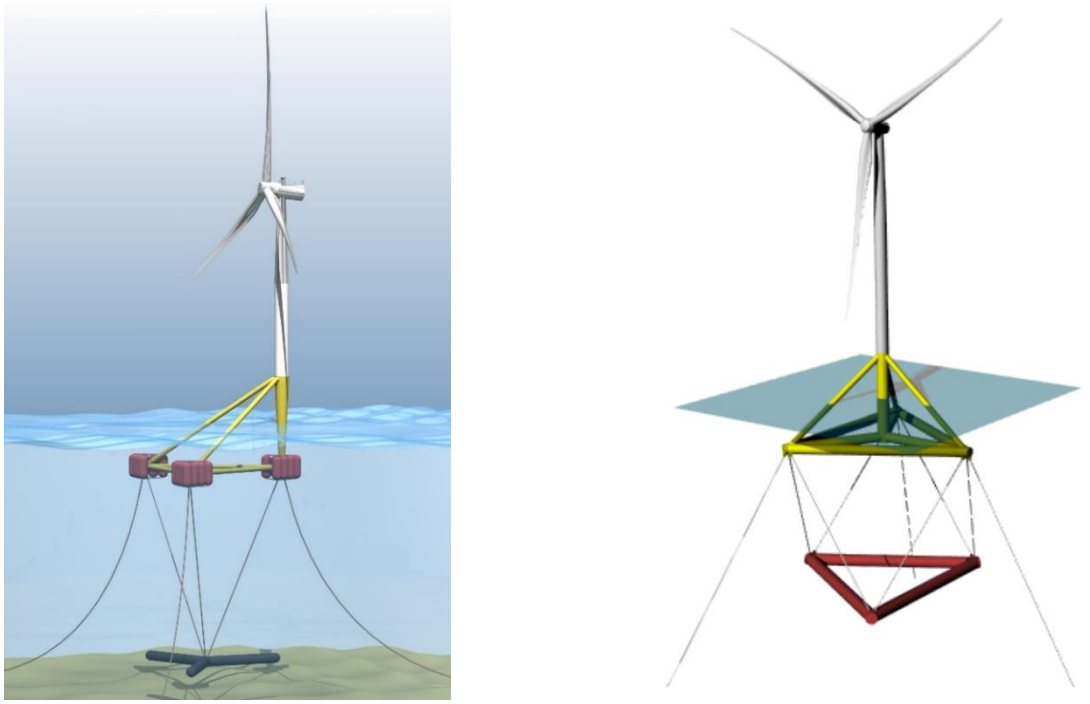

(a) (b)

Figure 1: Conceptual representation of the OrthoSpar (Barnes et al., 2017) (a), and the TetraSpar (Borg et al., 2020) (b).

Both concepts are designed to be fully installed onshore or at the port side – i.e., the floater platform will be assembled using land lifting equipment at the port side and then to assemble the wind turbine to the platform. Once the floater and wind turbine are assembled at the port, the full system could be towed unballasted to the installation site and fully installed by using small anchor handler vessels. The counterweight would be towed unballasted to the installation site and the attached to the floater platform before this is ballasted – For this reason this paper only considers the floater platform without the counterweight when studying the towing conditions.

3. MATERIALS AND METHODS

3.1. Physical model

For the experiments discussed here, a physical model based on a simplified version of the OrthoSpar FOWT prototype proposed by (Barnes et al., 2017) and previously built by (Zuzzalova, 2017) was used. The 1:50 scale model (Figure 2) was designed considering multiple parameters, such as: experience from previous models, available commercial materials, the capabilities of the experimental facility and the reference text (Hann and Perez-Collazo, 2018). Table 1 defines the most relevant dimensions of the model. Froude criterion and geometric similitude were considered when defining the scale model. To avoid unnecessary complexity in the manufacture of the scale model ballast tanks were simplified - i.e., by considering a single cylindrical body of the same buoyancy as in the prototype, instead of using multiple connected bodies. In addition to this, the lower section of the central tower was considered to have a constant diameter instead of a variable one. The NREL 5 MW turbine (Jonkman et al., 2009) was considered to define the characteristics of wind turbine, and represented in the scale model by a point mass positioned at the nacelle height (Abanades, 2019; Abanades et al., 2018).

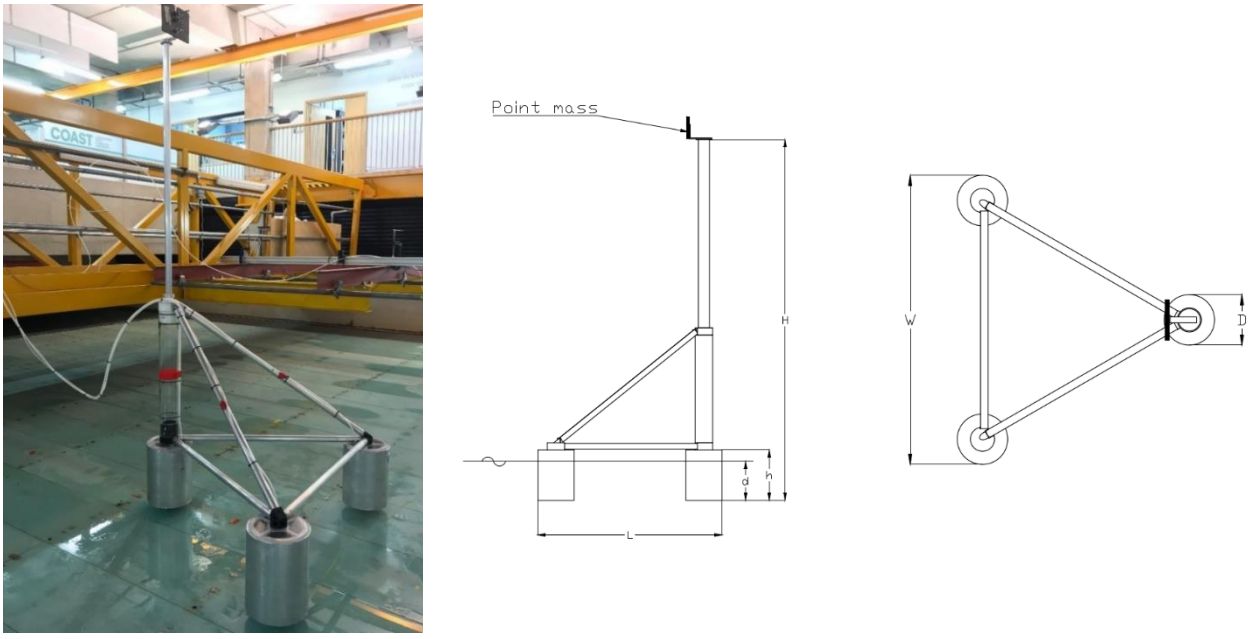

(a) (b) (c)

Figure 2: 1:50 scale model of the OrthoSpar concept: the model assembly at the University of Plymouth's COAST Laboratory (a) and a sketch showing the front view (b) and top view (c).

The purpose of this study is to understand the behaviour of the OrthoSpar during towing and seakeeping operations, where the counterweight is not ballasted and floats at the free surface under its own buoyancy. Therefore, the counterweight has not been considered for this study, as this will be installed later on once the platform arrives to its final destination.

The model was built of aluminium, methacrylate, nylon and Teflon (PTFE). Ballast tanks were manufactured out of a 3 mm thick aluminium plate, which was bended into a cylindrical shape and a bottom plate was welded to it. The upper lids of the ballast tanks were built out of a 10 mm thick methacrylate plate, and the central tower mast of the substructure was built out of a 60 mm diameter methacrylate pipe. The elements of the frame that link the ballast tanks with the central mast were built out of 38 mm diameter aluminium pipe. The wind turbine tower was built out of a 76 mm diameter aluminium pipe and connected to the substructure by means of a linking piece manufactured out of aluminium. Finally, the linking pieces for the different elements of the substructure were manufactured out of high resistance Nylon and Teflon. The need to adjust the water ballast level inside the ballast

tanks several times during the experiments –i.e., so to adjust the correct model draught and to raise the model out of the water at the end of every journey– required the design of a pneumatic ballast control system, which allowed an accurate levelling of the water ballast level at the inner tanks by adding or releasing compressed air into the tanks. Note that for this system to work, three nylon air hoses where carefully placed between the gantry and the model (Figure 2) ensuring that their effect on the dynamic behaviour of the platform was minimum, which was confirmed during the free oscillation tests (Appendix B).

Table 1: Main dimensions of the 1:50 model as tested in local coordinates and the full-scale prototype.

Parameter	**Symbol**	**Units**	**1:50 Model**	**Full-scale**
Length (x-dir)	L	m	1.290	64.5
Width (y-dir)	W	m	1.420	71
Height	H	m	2.500	125
Draft	D	m	0.270	13.5
Ballast tank height	H	m	0.370	18.5
Ballast tank outside diameter	D	m	0.270	13.5
Total mass (incl. ballast)	-	kg	45.300	2,265
Turbine mass	-	Kg	2.800	140
Total water ballast mass	-	Kg	19.000	950
Centre of gravity (z-dir)	-	m	0.096	4.8
Centre of buoyancy (z-dir)	-	m	-0.238	-11.9
Towing velocity	V	m/s	0.15 ~ 0.29	1.06 ~ 2.05
Reynolds number	Re	-	$4.03 \sim 7.8 \times 10^{4}$	$1.43 \sim 2.76 \times 10^{7}$
Froude number	Fr	-	$0.85 \sim 3.18 \times 10^{-2}$	
Cauchy number	Cy	-	0.204 ~ 0.763	

Once the model construction was complete, a hydrostatic and dynamic analysis of the scale model was carried out to validate its stability, ballasting and drag forces (Biran and Pulido, 2014) – see Appendix A for additional details. To reduce the draft to a minimum, the model was towed (see Section

3.1.1) in the lightest possible ballasting state – i.e., the central mast buoyancy tank is not ballasted, while the two fore buoyancy tanks contain enough ballast to counteract the off-centred mass of the tower and turbine. The resonance frequencies were found to be 0.411 Hz (0.058 Hz at prototype scale) in roll and 0.425 Hz (0.060 Hz at prototype scale) in pitch.

With a metacentric height of 0.5 m, the model was found to be very stable in the de-ballasted towing state at a draft of 0.27 m (13.5 m at prototype scale). With increasing ballast, the metacentric height reduces to 0.4 m, point this where the top of the ballast tanks begins to be fully submerged. With a further increase in ballast, the waterline decreases rapidly, resulting in a highly unstable condition. Small changes in the mass of water at each one of the ballast tanks produced large inclination angles requiring a precision adjustment of the ballasted water mass, so that the model's correct alignment was maintained. With the tanks fully submerged most of the buoyancy reserve of the platform was already used, while most of its mass is still present at a higher point at the wind turbine. This makes that, small changes in ballast mass tend lean the platform towards its lee, where the wind turbine is positioned. It is not the purpose of this study to further investigate this topic, as only the lightest possible ballasting state was of interest, and future research should further tackle this matter.

The design of the towing line considered: (i) the limitations of the experimental facility – e.g., dimensions, current and wave directions; (ii) industry guidelines (DNV GL, 2018b); and (iii) the reference text (Hann and Perez-Collazo, 2018). Froude and Cauchy similitude were considered to define the towing line, which was built out of a stainless-steel wire rope –when Froude and Cauchy similitude are applied these two non-dimensional numbers are keep constant at both scales (model and prototype), being their values in this case 0.85 ~ 3.18 x 10^{-2} and 0.204 ~ 0.763, respectively. A spring was used to simulate the elasticity of the full-scale towing line and scaled considering Cauchy similarity. As a reference for the full-scale towing line, an industry standard wire rope of the required minimum breaking load (MBL) was used – see Appendix C for further details.

The model was towed at a sub-critical Reynolds number of 4.03~5.92 x 10^4, at which the drag coefficient was assumed to be 1.1, resulting in a towing load of 5.6 N in still water. At the full-scale towing speed of 2 ~ 4 kn (1.06 ~ 2.05 m/s) the device would be towed at a supercritical Reynolds number of 1.43 ~ 2.76 x 10^7 instead. Following Fujiwara et al. (2013) it can be estimated that the full scale drag coefficient would be lower (asuming it to be 0.8), which leads to a full scale towing load of 521 kN.

3.2. Experimental set-up and testing programme

3.2.1. Wave basin

The physical model testing was conducted in the ocean basin at the University of Plymouth's COAST Laboratory, which is able to generate waves and currents simultaneously. The dimensions of the basin are 35 m x 15.5 m with 24 independent hinged-flap wave paddles. An active wave absorption system of the paddles and a parabolic beach help to reduce settling time and increase the accuracy of the produced waves. Being the reflection coefficient below 10% for the range of wave frequencies tested in this research (Collins et al., 2015). The basin is equipped with bi-directional pumps, able to generate both, longitudinal and transverse currents of up to 0.3 m/s. Turbulence intensities of the flow were calculated as described by (Hann and Perez-Collazo, 2018) from the data measured by the current meters during current-only conditions (Set A) and found to be in the range of 12.1 % to 17.9 %. In addition, turbulence integral length scales were also calculated as described by (El-Gabry et al., 2014) and found to be in the range 4.7 ~ 8.8 x 10^{-2} m, being these an order of magnitude smaller than ballast tanks diameter, therefore, turbulence of the generated current would not excite the floating structure. The water depth, of the testing area section was set to 1.2 m.

3.2.2. Instrumentation

Multiple time series from various instruments were recorded for each test run. Seven conductive wave gauges (WGs) were used to measure the free surface elevation along the wave basin. Current

flow was measured by means of two 2-axis electromagnetic current meters (Valeport Ltd., Model 802, Sensor: Discus 3.2), capturing the longitudinal (x-direction) and transverse (y-direction) flow components. A Qualisys® optical tracking system with 8 cameras was used to measure the motion of the model in its 6 degrees of freedom (6 DoF) (Hann and Perez-Collazo, 2018). Reflectors were attached to the top of the tower to ensure a good visibility by the cameras, regardless of the model orientation. Then the recorded motions were translated to a local coordinate system. Furthermore, to record the load on the towing line, an in-line tension and compression load cell (Applied Measurements Ltd., DDENA1S-500N-C8) was placed between a fixed point connected to the gantry and the towing line spring. To increase redundancy and accuracy, a 635 mm string pot (TE Connectivity, SM2-25) was installed to measure the extension of the spring, which could then be converted according to its calibration curve to the force acting on the spring – i.e., the towing load.

3.2.3. Layout

The origin of the global coordinate system was defined on the still water level, centreline and at a distance of 15.6 m from the wave paddles. The x-axis was oriented towards the beach, the y-axis towards the left hand-side basin wall (as seen from the paddles) and the z-axis upwards. A local coordinate system was defined with its origin in the centre of the three buoyancy tanks (vertically above the centre of gravity) and on the level of the tank tops with its x-axis pointing opposite the towing direction, the y-axis starboard and the z-axis upwards.

Instead of towing the model through the basin, it was kept stationary while a current was generated in the basin, following (Chakrabarti, 1998; Villaespesa et al., 2018). This method made infinitely long test runs possible. The fore tugboat was simulated by connecting the towing line to a lightweight Dyneema rope (~1 g/m), which was deflected upwards by a fixed pulley located 9 m in front of the model and 6 cm above the still water level (Figure 3). The Dyneema rope was connected to a spring (0.08 N/mm) which was attached to a fixed load cell. The simulation of an aft tugboat was necessary to prevent the model from extensive sway movements. It was simulated by a constant force of 1.6 N

(resembling 20 tons of bollard pull at full scale) being applied towards a fixed point in the basin. This was done by connecting the model to a weight by a Dyneema rope via two pulleys 6 cm above the still water level (Figure 3).

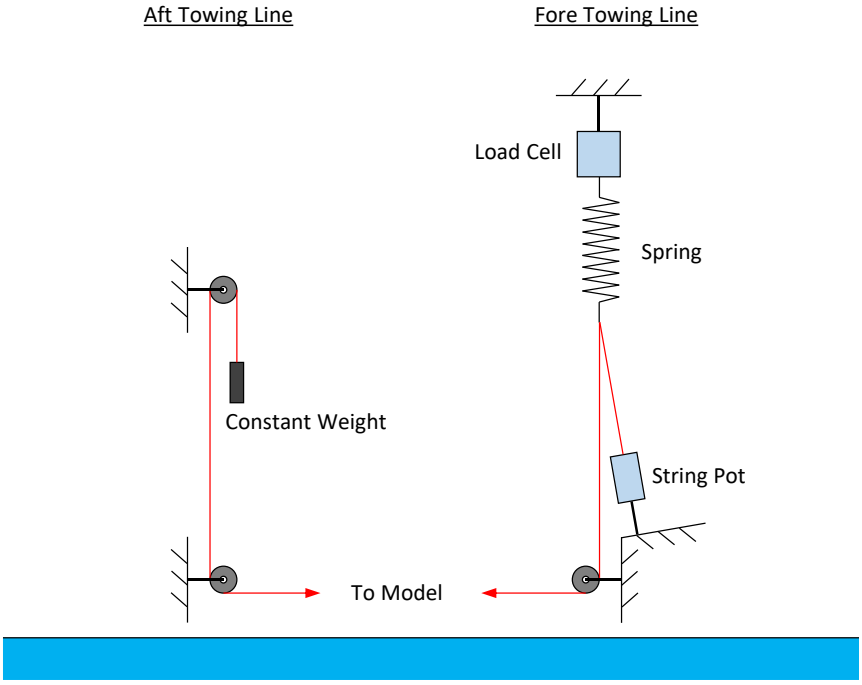

Figure 3: Setup of the towing line connection points.

As four different orientations of the model towards the waves were investigated, four of the described fore and aft line connection points were defined prepared prior testing. Figure 4 shows the experimental setup with the global coordinate system and the model orientated at 0°. Furthermore, Table 2 defines the global coordinates of the model, connection points and instrumentation.

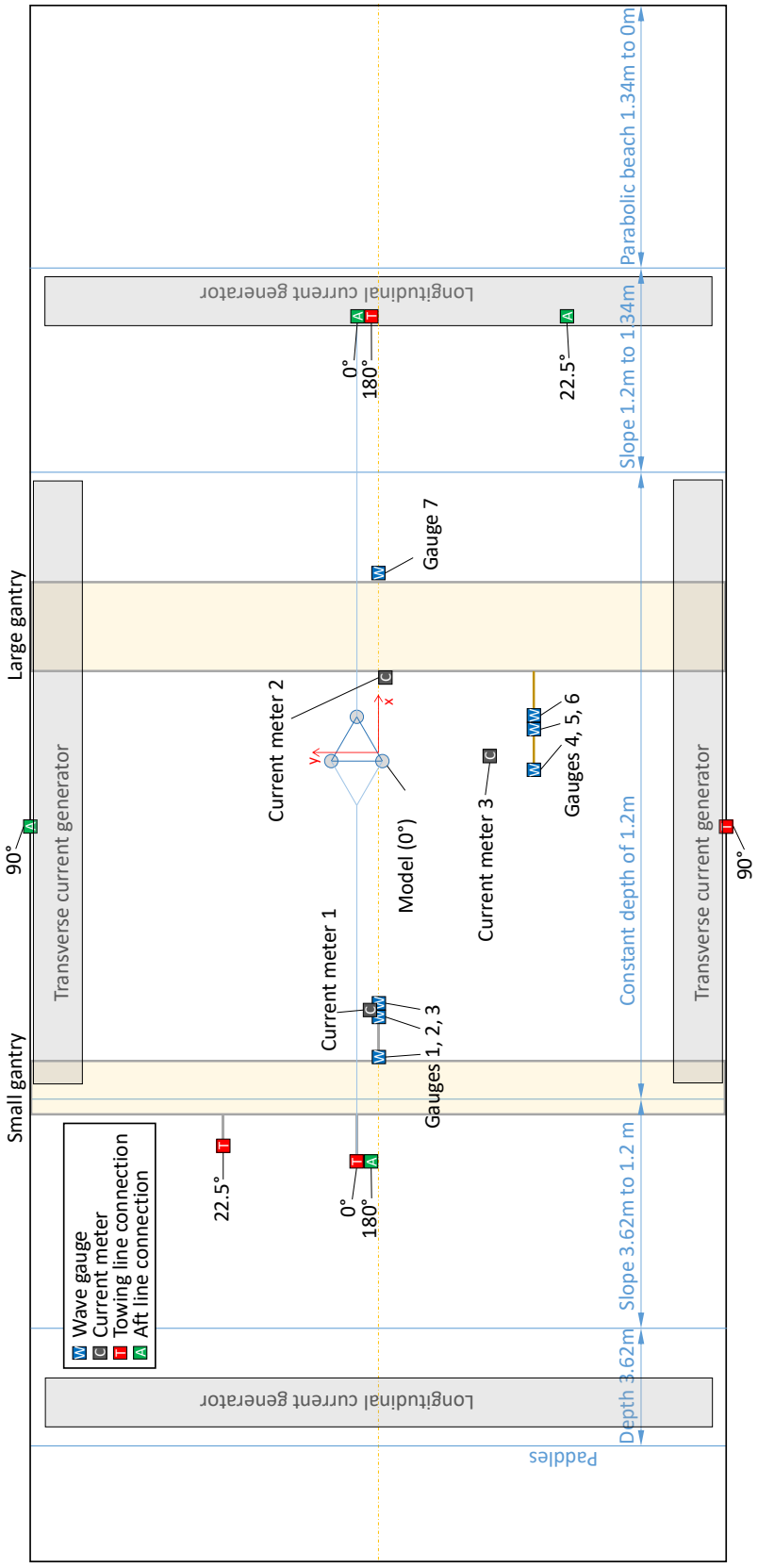

Figure 4: Experimental set-up.

Table 2: Global coordinates of the model, connection points and instrumentation.

Part	Setup	X-coordinate	Y-coordinate
Model	0°	0.17 m	0.5 m
	90°	-1.67 m	1.56 m
	180°	0.47 m	0.5 m
	22.5°	-0.2 m	-0.1 m
Towing line connection	0°	-9.2 m	0.5 m
	90°	-1.67 m	-7.77 m
	180°	9.8 m	0.5 m
	22.5°	-8.85 m	3.5 m
Aft line connection	0°	9.8 m	0.5 m
	90°	-1.67 m	7.77 m
	180°	-9.2 m	0.5 m
	22.5°	9.8 m	-4.25 m
Wave gauge 1	all	-6.85 m	0 m
Wave gauge 2		-5.95 m	0 m
Wave gauge 3		-5.65 m	0 m
Wave gauge 4		-0.37 m	-3.5 m
Wave gauge 5		0.53 m	-3.5 m
Wave gauge 6		0.83 m	-3.5 m
Wave gauge 7		4.03 m	0 m
Current meter 1	0°	-5.8 m	0.2 m
Current meter 2	90°, 180°	1.68 m	-2.5 m
Current meter 3	0°, 90°, 180°	-0.07 m	-0.15 m

The instruments described in Table 2 were installed as shown in Figure 4. Two sets of three wave gauges were placed in front and to the side of the model relative to the wave direction. Each one of

these sets of three wave gauges was used to record the input signals for an incident and reflected wave analysis, following (Perez-Collazo et al., 2019). The eight Qualisys cameras were located at the side of the tank in positive global y-direction. Therefore, the reflectors needed to be attached to the model in a place where they would be visible for the cameras to calculate the movements. Considering the rotation of the model for different setups, the most suitable location to attach the reflectors was chosen to be the top of the tower (z = 2.13 m). In order to record the current flow, two current meters were installed to the front and to the side of the model relative to the current direction. As the current direction varied for different sets, the location of one current meter was changed after set C. The current meters were measuring the flow at 13 cm below the still water level, which represents half of the draft of the model's buoyancy tanks.

3.2.4. Experimental programme

The first tests of the experimental programme were free oscillation tests of roll, pitch and heave to measure the resonance frequencies of the device as proposed by (Hann and Perez-Collazo, 2018). The resonant frequencies were found to be of 0.408 Hz for roll, 0.410 Hz for pitch and 0.843 Hz for heave. For the range of spectral frequencies to be investigated in this research (0.366 Hz to 0.629 Hz) heave resonance was not expected to interfere with the results. The average damping ratio was calculated by the logarithmic decrement (Turunen et al., 2011) and found to be 2.1 % for roll and 2.72 % for pitch. For further details on the calculation, see Appendix B.

To investigate the influence of the directionality of the waves, the model was positioned at four different orientations with respect to the wave paddles (0°, 22.5°, 90° and 180°). Note that the direction marking 180° means that currents were circulating from the dissipation beach to the wave maker, while for the direction 90°, currents were circulating transversally to the wave basin. The different setups were investigated in wave-only and combined wave and current conditions. Additionally, one set of currents-only was tested at 0° under three different current velocities – 0.15, 0.22 and 0.29 m/s (2, 3 and 4 kn at full scale, respectively). Table 3 shows the nine resulting experimental sets.

Table 3: Description of tested sets (model scale).

Set	Setup	Currents [m/s]	Wave height [m]
A	0°	0.15, 0.22, 0.29	-
B	0°	0.22	0.04
C1	0°	-	0.02
C2	0°	-	0.04
D	90°	0.22	0.04
E1	90°	-	0.02
E2	90°	-	0.04
F	180°	0.22	0.04
G	22.5°	-	0.02

The frequencies of the tested waves were chosen in relation to the resonant frequency of the dominating rotational movement of the setup with a range from 0.366 Hz to 0.628 Hz (period of 19.34 s to 11.26 s at full scale). Within each set, one run was at resonant frequency, three runs below and five runs above the resonant frequency were performed. Each regular wave run consisted of 100 waves. Furthermore, one run of irregular waves at resonant frequency and a duration of 510 s was defined – to resemble 1h at full scale – and included in setups B, D and F. If currents were used in a set, these were kept running in between runs of the set to ensure a constant turbulence intensity.

3.2.5. Repeatability tests

To prove the repeatability of the experiment, runs of the sets C2 (0°) and E2 (90°) were repeated twice each, resulting in two sets of three runs. The normalised root mean squared error (*NRMSE*) and the correlation coefficient R^2 were calculated, comparing the seven wave gauges, roll, pitch and the towing line load between the three runs. Table 4 shows the NRMSE and correlation coefficients averaged over the three runs.

Table 4: Averaged *NRMSE* and R^2 values of wave gauge, roll, pitch and towing load data of the 0° and 90° setup.

Parameter	*0 deg*		*90 deg*	
	R^2	*NRMSE*	R^2	*NRMSE*
Wave Gauge 1	0.999	0.38 %	0.999	0.30 %
Wave Gauge 2	0.999	0.41 %	0.999	0.31 %
Wave Gauge 3	0.999	0.40 %	0.999	0.36 %
Wave Gauge 4	0.999	0.69 %	0.999	0.59 %
Wave Gauge 5	0.999	0.55 %	0.999	0.49 %
Wave Gauge 6	0.999	0.53 %	0.999	0.47 %
Wave Gauge 7	0.999	0.52 %	0.999	0.41 %
Roll	0.999	1.14 %	0.999	0.42 %
Pitch	0.998	1.35 %	0.998	1.33 %
Towing Line Load	0.984	4.65 %	0.005	26.35 %

The best repeatability was found for the water surface elevation as measured by the wave gauges with all *NRMSE* values below 0.7 % and the lowest R^2 at 0.999. With the *NRMSE* values up to 1.35 % and the lowest R^2 at 0.998, the rotational movements were also found to be highly repeatable, although less than the waves. The repeatability of the towing line load depends on the direction of the waves, with a sufficient repeatability at 0° (4.56 % and 0.986) and no repeatability at 90° (26.35 % and 0.0049). This is attributed to the vanishing towing line loads in waves from the side, resulting in a random time series, where no regularity could be distinguished.

3.3. Data analysis

The reflected wave analysis proposed by (Mansard and Funke, 1980) and modified later by (Baquerizo et al., 1998) was applied to the free surface elevation recorded at each one of the two groups of three wave gauges – 1, 2 and 3; and 4, 5 and 6 respectively (Figure 4). Reflection coefficients ranging from 0.11 to 0.49 were obtained and these values lie within the expected range for the type of wave basin and wave frequencies studied. On the basis of this reflection analysis, the incident wave height obtained from wave gauges 4, 5 and 6 was used to calculate the incident wave height at the

average position of the centre of buoyancy of the model – note that this interpolation is important to reduce errors when calculating the different motion responses to the incident wave height.

Based on the incident wave height (H_i) and on the motions of the FOWT, recorded by the 6-DOF tracking system Qualisys, the response amplitude operator (RAO) for roll and pitch (RAO_{roll} and RAO_{pitch}, respectively) were determined following (Lopes, 2011).

$$RAO\ (f) = \frac{A_0 l^k}{H_i} \tag{1}$$

where A_0 is the peak-to-peak amplitude of the recorded angular motion in radians, *l* is the characteristic dimension of the model (model width (1.423 m) for roll and the model length (1.288 m) for pitch), and *k* is an exponent which is zero for the translation modes and 1 for the rotation modes, thus 1 for these experiments.

As the submerged part of the model is of symmetric equiangular triangular shape, motion response of the FOWT to pitch and roll could be transformed about the main axes in 60° steps, for the test sets where towing was not involved – i.e., sets C1, C2, E1, E2 and G. For instance, motions which are experienced at 90° could be transformed to 30°, as the second moment of inertia is equal.

Transformation about an angle α was carried out according to Equations (2) and (3).

$$RAO_{\alpha,roll} = RAO_{roll} \cdot \cos(\alpha) - RAO_{pitch} \cdot \sin(\alpha) \tag{2}$$

$$RAO_{\alpha,pitch} = RAO_{pitch} \cdot \cos(\alpha) + RAO_{roll} \cdot \sin(\alpha) \tag{3}$$

The combined RAO was calculated as the vector sum of roll and pitch RAO's via Equation (4). It was calculated for all measured and transformed RAO's.

$$RAO_{comb} = \sqrt{{RAO_{roll}}^2 + {RAO_{pitch}}^2} \tag{4}$$

4. RESULTS

4.1. Motion response

In this section, the motion response of the OrthoSpar FOWT to the incident wave field is analysed by means of the response amplitude operator (RAO) for both roll and pitch angular motions. The recorded motions in heave, for the test sets considered in this research, were shown to be very small, hence the response in heave is not considered to be relevant for the purposes of this study. Next, the influence of wave height, wave direction and towing over both roll and pitch RAOs is analysed.

4.1.1. Influence of Wave Height

The influence of the wave height on the RAO is presented in Figure 5, which shows the roll and pitch RAOs for a 2 and 4 cm incident wave height (1 and 2 m at prototype scale, respectively) and for two different experimental setups (0° and 90° without towing). Here, trend-lines have been plotted to ease the interpretation of the results but do not resemble measured or calculated data.

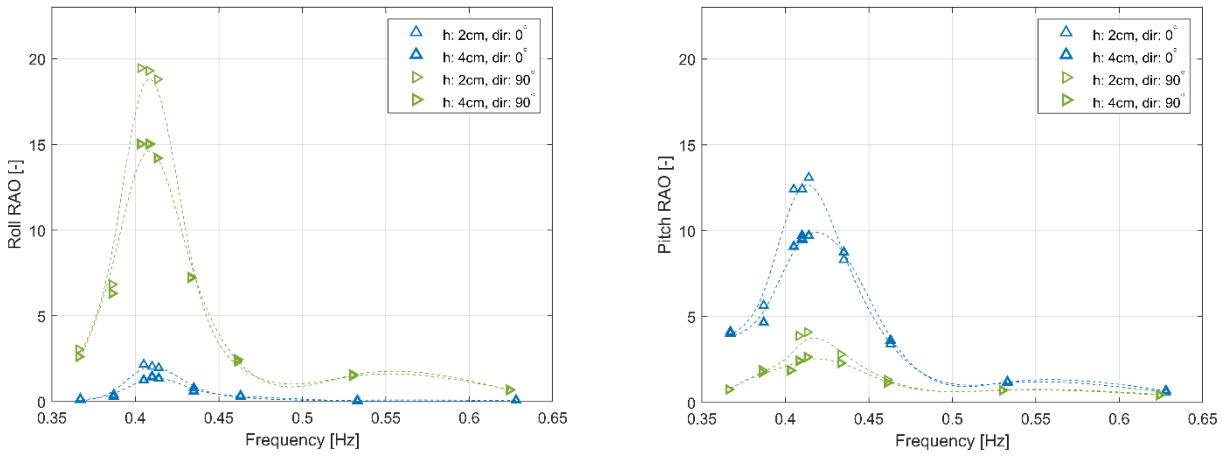

(a) (b)

Figure 5: Influence of the incident wave height on: (a) roll RAO and (b) pitch RAO; (data at model scale).

It is clear from Figure 5 that maximum values for both angular motions (roll and pitch) occur at their respective resonance frequencies (see Section 3.1) and that for wave frequencies larger than 20% of the resonance ones, both RAOs are reduced greatly. Both, pitch and roll RAOs show a strong influence of both, wave direction (see next section) and wave height, showing this last one a reduction

of the response in the resonant frequency of about 25% for both orientations (0º and 90º) when the incident wave doubles its height.

As expected, the roll RAOs are generally higher due to the reduced moment of inertia of the water plane area (Equation A.2) around the local x-axis. The trend of the RAOs over varying requested wave frequencies shows distinct peaks at about 0.408 Hz for roll and 0.414 Hz for pitch. This observation confirms the results of the free oscillation tests (0.408 Hz and 0.410 Hz) as well as the results of the hydrodynamic analysis (0.411 Hz and 0.425 Hz) (Section 3.1).

4.1.2. Influence of the wave direction

As outlined in the previous section, the incident wave direction shows an important effect on both roll and pitch RAOs. To understand further the effect that the wave direction has on the response of the device, roll and pitch RAOs are plotted in Figure 6 for the three directions tested in the experimental campaign (0º, 22.5º and 90º). The Figure shows that, generally, the OrthoSpar response in roll increases from 0° to 90° while the response in pitch decreases.

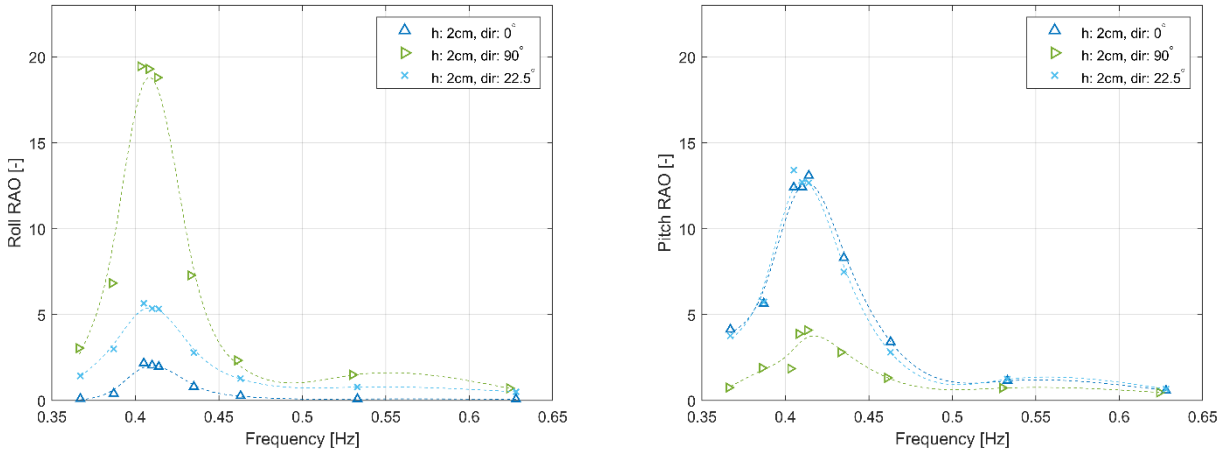

(a) (b)

Figure 6: Influence of the incident wave direction on: (a) roll RAO and (b) pitch RAO; (data at model scale).

To understand the effects of the wave direction on the OrthoSpar response, as explained in Section 3.3, Equations (2) and (3) were used to obtain the respective roll and pitch RAOs for the complementary angles to those tested (i.e., 30º, 37.5º, 60º and 82.5º), which are plotted in Figure 7.

Both, roll and pitch RAOs show peaks at the same frequency (0.405 Hz). As seen, above, the response of the device in roll shows its minimum values for a 0º direction, while its maximum values correspond to the 90º direction. In general, roll RAO values increase from 0º to 90º, showing two maximum RAOs, the first at 90º and the second at 30º. The reason for the occurrence of the second maximum at 30º is because this is transformed from the 90º RAO. Furthermore, the response of the device in pitch shows, as for roll, two maximum RAOs, the first at 30º and the second at 22.5º. Overall, there is a clear difference in the response in pitch observed for incident wave directions less than 37.5º than for those with a larger angle, where the pitch motions are reduced considerably.

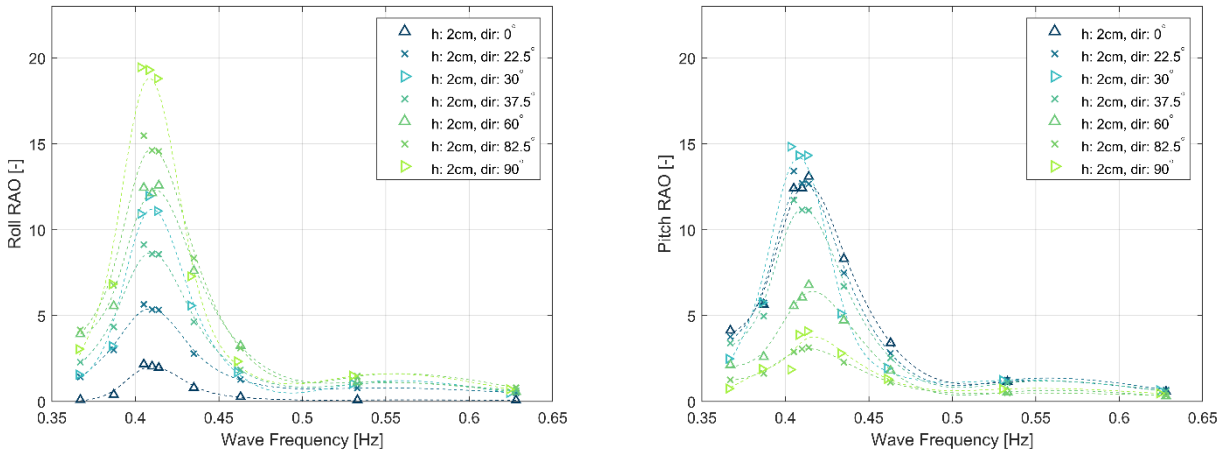

(a) (b)

Figure 7: Influence of the incident wave direction on: (a) roll RAO and (b) pitch RAO; (data at model scale).

When considering towing and sea-keeping operations at sea, the FOWT real response would be a combination of both roll and pitch responses. For this reason, Figure 8 plots the combined roll-pitch response, using Equation (4), as defined in Section 3.3. The combined RAO clearly identifies two maximum values of the RAO, the first at 90º and the second at 30º, reducing in value towards the 0º direction where the minimum RAO values are found. The results show, that the RAOs at incident wave directions of 30° and 90° (and also 150° accordingly) are about 35% higher than those at other wave directions.

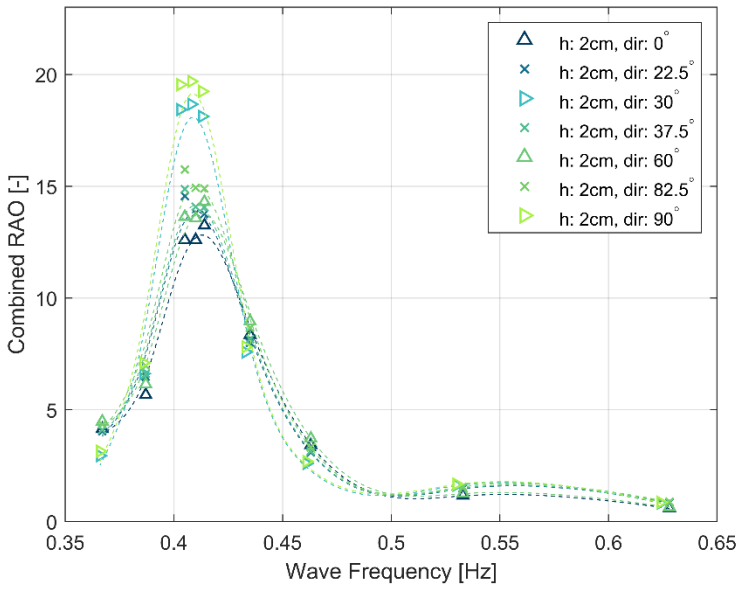

Figure 8: Combined RAO's over 90° of wave direction (data at model scale).

4.1.3. Influence of towing

Here we analyse the response of the OrthoSpar in roll and pitch under tow. Figure 9 presents both roll and pitch RAOs for a 4 cm wave height (2 m in prototype scale) and three different towing directions (0º, 90º and 180º). It should be noted that the towing directions are simulated by using currents in the wave basin, for this reason, test cases for 180º and 90º directions are equivalent; when currents are not present, RAOs for the 180º direction can be transformed from the 90º one.

Figure 10 shows a clear influence of the towing on both, roll and pitch RAOs, in particular near the resonant frequencies. The peak RAOs were reduced by 19 % when towing at 90° and by 17 % at 0° and 180°. Influences on the RAOs were observed at different ranges of frequencies depending on the orientation. At 0°, the pitch RAO was reduced at the resonant frequency and below (0.366 Hz to 0.414 Hz) the trend appears to have shifted to higher frequencies. At 90°, the roll RAO was reduced only around the resonant frequency (0.403 Hz to 0.414 Hz) and no shift occurred. At 180°, the pitch

RAO was reduced around the resonant frequency (0.405 Hz to 0.435 Hz), while it increases for higher frequencies (0.463 Hz to 0.629 Hz).

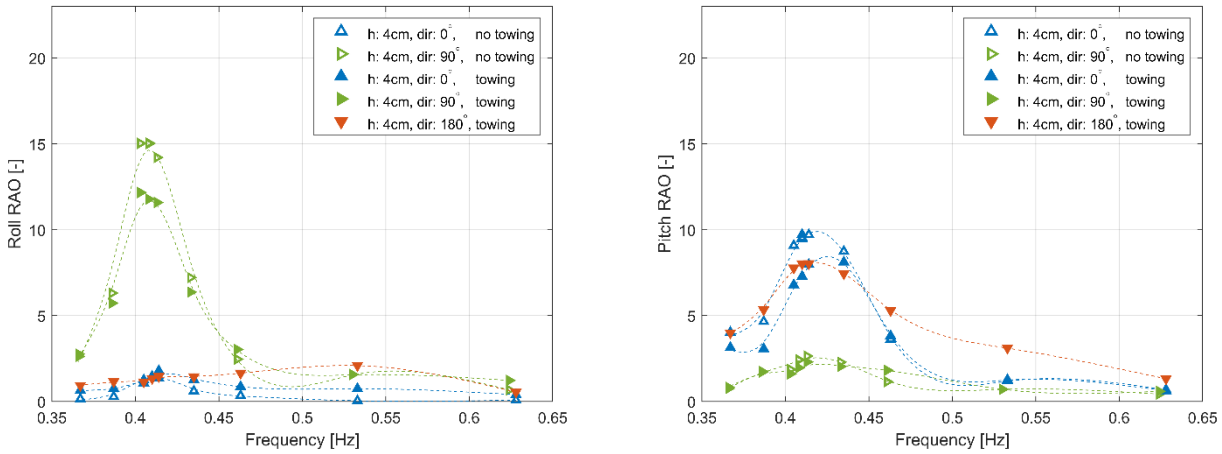

(a) (b)

Figure 9: Influence of towing on: (a) roll RAO and (b) pitch RAO; (data at model scale).

When an object is being towed through waves, the wave period it experiences, is dependent on the towing speed and heading in relation to the wave direction as observed by (Amante et al., 2016). When towing is simulated with a stationary model in currents, the wave period acting on the model will be constant regardless of the towing speed or direction – as the current may have an effect on the wave steepness but not a significant one on the wave period. Experimental results may be expressed in relation to the apparent period (as tested) or in relation to the real wave period (when towed). The apparent wave period T_{ap} was transformed to the real period T_r as follows

$$T_r = T_{ap} \cdot \frac{v_w + v_t}{v_w} \tag{5}$$

where, v_w is the velocity of the tested waves and v_t is the towing velocity. Figure 10 account for this error, showing the response in roll and pitch that the model would experience under real towing conditions. The figure shows that although the corrected RAOs for roll are very similar to the ones in Figure 9, when it comes to the pitch RAO, there is a significant difference, as now RAOs for 0º and

90º are shifted. When towing at 0ª the peak of rolls RAO is shifted to lower frequencies while when doing it at 180ª, this is shifted to higher frequencies.

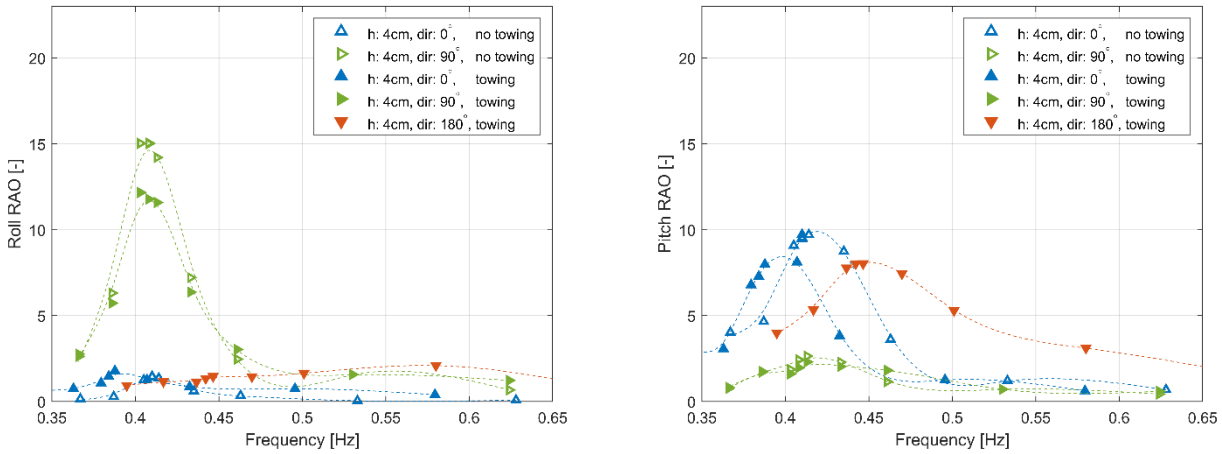

(a) (b)

Figure 10: Influence of towing, for a moving model, on: (a) roll RAO and (b) pitch RAO; (data at model scale)

4.2. Towing load

The peak-to-peak amplitude of the dynamic towing load (F_0) describes the variation of the towing line load during any test run. Figure 11 shows the load amplitude for 0°, 90° and 180°, where the amplitude has been normalised with the wave height (H), the density of the water (ρ) and the gravitational acceleration (g). For comparative purposes, the loading amplitude measured at the towing line without currents is also plotted for 0°.

It is clear from Figure 11 that direction is the main parameter influencing the towing load, at 180º direction larger loads are produced, while the lowest values are found for 90º. Furthermore, the figure shows in most cases that a clear peak, when analysing the effect of the wave frequency on the towing load. The maximum load values can be observed for the peak occurring at 0.435 Hz (T = 2.30 s). In addition, a minimum can also be observed, in general, at 0.387 Hz (T = 2.58 s). The results show that load values are about 40% larger, in average, when towing at 180° compared when doing it at 0°, notwithstanding, towing at 90° shows load values that are, in average, about 85% lower than at 0°.

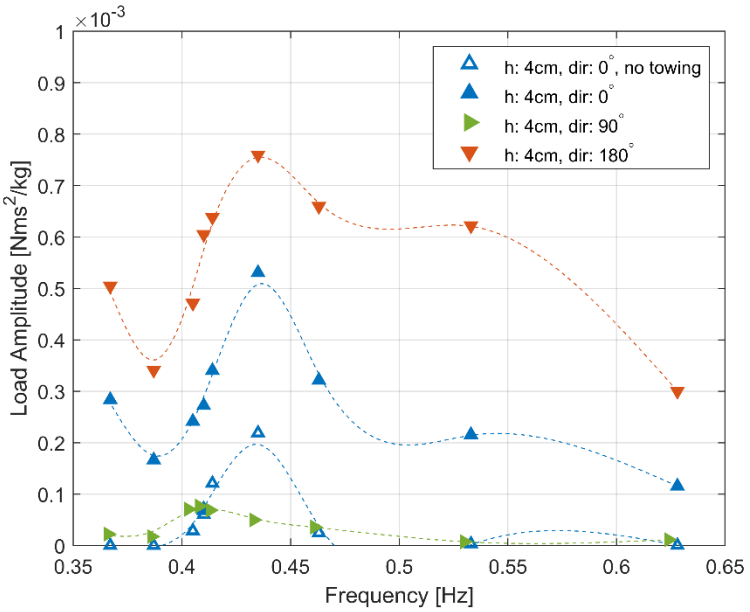

Figure 11: Peak-to-peak amplitude of the towing load (data at model scale).

To understand the behaviour of the towing load, it is not enough to compare this with the response of the OrthoSpar in pitch while being towed (Figure 9b), as the towing load is not only a result of pitch motion, but also of surge motion. For this reason, the influence of the towing direction on the surge amplitude is plotted in Figure 12.

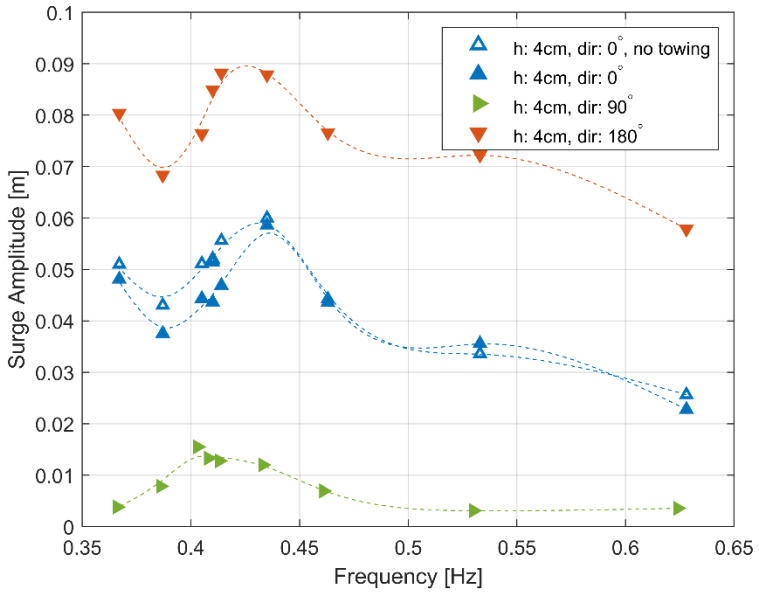

Figure 12: Influence of the towing direction on the surge amplitude (data at model scale).

5. DISCUSSION

In this work, a scale model of the OrthoSpar FOWT concept is studied at its transport phase – i.e., while this is being towed de-ballasted. In particular, the motion response of the device and the measured loads on the towing line, for different sea conditions, wave heights and wave directions are studied here. Results of an experimental campaign of a simplified model of the OrthoSpar FOWT in the towing state were presented. The roll and pitch motion response of the device in three different orientations to the waves (0°, 22.5° and 90°) was examined. Towing load characteristics have been analysed during towing at three different wave angles (0°, 90° and 180°).

In general, the RAOs showed a pronounced peak at the expected resonant frequencies with high responses. At wave frequencies only 9 % above or below the resonant frequency, the responses were reduced by 75 % in roll and 60 % in pitch. Thus, it is recommended to strictly avoid resonant wave frequencies in the de-ballasted condition. In terms of the influence of the wave height, a non-linear relation of the RAO was found. Both, roll and pitch motion response increased by 25 % in halved wave heights. Even indistinguishable wave heights near the resonant frequency would result in severe roll and pitch motions. This effect can be explained by the increased viscous damping of the buoyancy tanks in higher velocities due to larger waves.

When assessing sea conditions for towing, the wave frequency is of higher importance than the wave height in relation to rotational movements. As expected, the orientation of the device towards the incident wave direction has an influence on roll and pitch response. Due to the triangular shape of the structure, the combined peak RAOs were found to increase by 35 % at incoming wave angles of 30°, 90° and 150° compared to other angles. Therefore, orienting the device at those angles towards the waves should be avoided. As an effect of towing, it was found that the peak RAOs decrease by 17 % to 19 % compared to the stationary condition.

The towing load was characterised by means of the peak-to-peak amplitude of the dynamic towing load. It was found that the angle between the towing direction and the incident waves greatly influences

the loads measured at the towing line. At an angle of 180°, the most adverse load characteristics were identified with the load amplitude at least 40 % higher than with towing at 0°. On the contrary, at an angle of 90°, the lowest load characteristics were observed, with load amplitudes of about 85% lower than when towing at 0°. Comparing the three figures (Figures 9b, 11 and 12) it can be noted that the peaks observed at 0.435 Hz (Figure 11) were shifted above the resonant pitch frequency at 0.410 Hz (Figure 9b). When analysing the significant surge amplitude, (Figure 12) reveals a similar shift and overall shape, also showing the same minimum at 0.387 Hz. Finally, the difference observed at larger wave frequencies for the 180º direction, in comparison with the other directions, can be explained by the behaviour observed for the 180º pitch motion at larger frequencies (Figure 9b).

6. CONCLUSIONS

This work tackles the physical model testing of the OrthoSpar, a novel concept of FOWT, through an intensive experimental campaign at the University of Plymouth's COAST Laboratory. In the experimental campaign, three aspects were investigated: (i) the platform seakeeping under different wave climates and directions, where the natural frequencies of the platform motions modes were identified; (ii) the stability of the platform when being towed; and (iii) the effect that different wave climates and directions would have on the towing line load.

Based on the analysis of the results from this work the following main conclusions may be drawn:

- The OrthoSpar resonance frequencies were found to be 0.411 Hz in roll and 0.425 Hz in pitch (0.058 and 0.060 Hz at porotype scale, respectively).
- The seakeeping study was carried out by analysing the pitch and roll motions of the platform using the RAO under different sea states and wave directions.
- The relationship between wave height and the RAO leads to the conclusion that even small wave heights can result in extensive rotational movements, especially near resonant frequencies.

- In general, the rotational RAOs were high with distinct peaks. A consequence of this should be the avoidance of the resonant wave frequencies during towing and installation. A reduction of 75 % in roll and 60 % in pitch RAO could be achieved by a variation of 9 % from the resonant frequency.
- The results show, that the RAOs at incident wave directions of 30° and 90° are about 35% higher than those at other directions, as result of the triangular shape of the platform. It is recommended to avoid those wave directions during offshore operations, especially in long waves, e.g., by slightly changing the orientation of the device, or avoiding operations in the given conditions.
- The stability of the FOWT while being towed was analysed by means of the RAO, showing that the wave direction has a strong influence on the turbine stability, in particular for frequencies around the resonance peaks. The roll RAO was particularly influenced by the 90° incident wave direction, while the 0° and 180° directions showed a larger influence on the pitch RAO.
- The dynamic loads on the towing line were studied while the FOWT was being towed under different conditions. It was observed that the loads measured in the line for the 90° direction were considerably lower than for the other two directions.

An important characteristic of any FOWT concept, which is ballasted during its installation, is the de-ballasted transport phase, where the FOWT is towed from an assembly location at the coast to its final production site. As the FOWT is de-ballasted, its hydrostatic and dynamic stability may vary greatly from those during operational conditions, therefore, the behaviour of the device during its transport phase should be carefully assessed, not only to design and plan the maritime operations of the transport, but also during the design phase of the FOWT itself.

ACKNOWLEDGEMENTS

This work was carried out as part of an MSc thesis project. The model used for the experimental campaign was constructed on a previous year with the financial support of a Research scholarship from the Santander Bank. This work was carried out with the financial support of the School of Engineering, Computing and Mathematics of the University of Plymouth. The Authors are grateful to Sam Strivens, and the University of Plymouth's COAST Lab technical staff for their support during the experimental campaign.

APPENDIX A. HYDROSTATIC AND DYNAMIC ANALYSIS

To carry out this analysis, the individual parts of the model were measured, weighed and the centre of gravity KG was determined. Small parts like vents, hooks or screws were neglected to simplify the calculations. Hydrostatic and dynamic analysis was carried out according to (Biran and Pulido, 2014). The metacentric height GM for roll and pitch was calculated according to Equation (A.1).

$$GM = KB + BM - KG \tag{A.1}$$

where KB is the height of the centre of buoyancy, KG is the height of the centre of gravity and BM the distance between the centre of buoyancy and the metacentre

$$BM = \frac{I_{WL}}{\Delta} \tag{A.2}$$

where I_{WL} is the second moment if inertia of the water plane area depending on the axis of rotation and Δ is the displacement of the model. The stability was further reduced due to free surface effects of the ballast water in the buoyancy tanks according to Equation (A.3).

$$dGM = \frac{3 \cdot I_T}{\Delta} \tag{A.3}$$

where I_T is the second moment of inertia of the circular inside area of the buoyancy tanks.

The natural roll and pitch periods were calculated as described in Equation (A.4).

$$T_N = \frac{2 \cdot \pi \cdot R}{\sqrt{g \cdot GM}} \tag{A.4}$$

with the radius of gyration

$$R = \sqrt{I_2 \,/\, \nabla} \tag{A.5}$$

where, I_2 is the second moment of inertia of the whole structure and ∇ equals the displaced volume. The drag force F_D of the model was calculated for different towing speeds according to Equation (A.6).

$$F_D = 3 \cdot 0.5 \cdot \rho \cdot v^2 \cdot c_p \cdot A_P \tag{A.6}$$

where, ρ is the density of the water in kg/m^3, v is the towing velocity in m/s, c_p is the drag coefficient of a cylinder according to (Fujiwara et al., 2013), and A_P is the submerged projected area in towing direction. The drag coefficient c_P depends on the Reynolds number Re

$$Re = \frac{\rho \cdot v \cdot D_T}{\mu} \tag{A.7}$$

where, D_T is the outside diameter of the buoyancy tanks and μ is the dynamic viscosity of the water.

APPENDIX B. FREE OSCILLATION TESTS

Three tests were carried out in each direction (roll, pitch and heave) to receive more reliable results. Figure 13 and Figure 14 show the exemplary time series of a free oscillation test of roll and pitch with the oscillation envelope. The resonant frequencies were calculated in the time-domain by zero up-crossing and the results were averaged. The NRMSE of the resonance frequencies were all below 0.23 %, with the averages at 0.06 % for roll and 0.15 % for pitch. From the free oscillation tests, the damping ratios of the model were calculated for roll and pitch according to the logarithmic decrement method as explained by (Turunen et al., 2011). The damping ratios were much more inconsistent with the average NRMSE at 7.8 % for roll and 5.6 % for pitch.

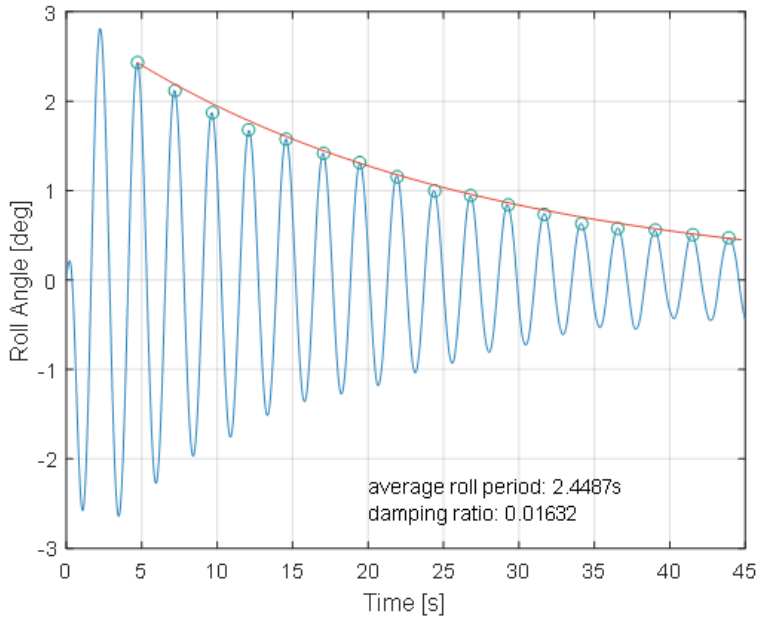

Figure 13: Example of time series of free oscillation test in roll.

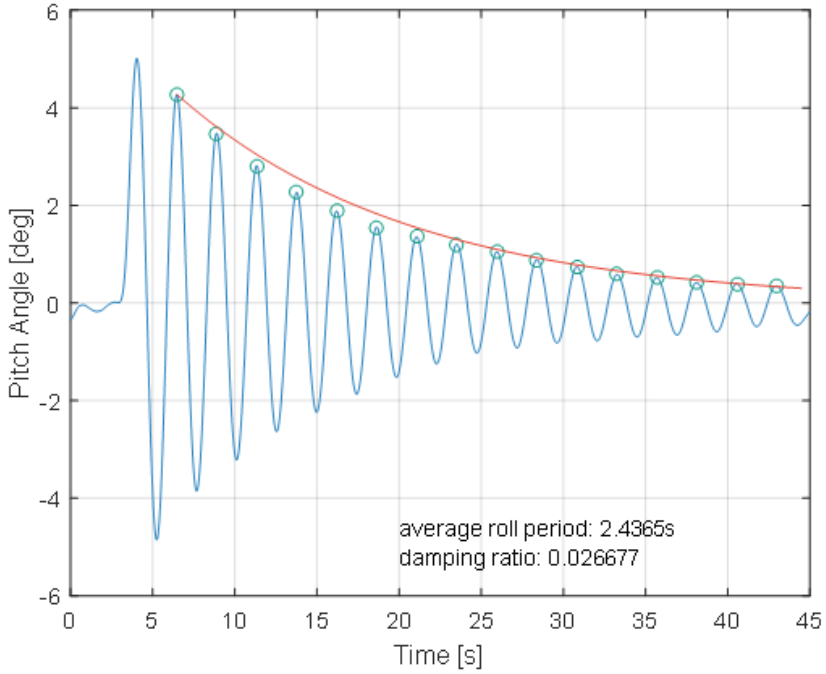

Figure 14: Example of time series of free oscillation test in pitch.

APPENDIX C. TOWING SISTEM DESIGN

For the design of the towing line it was assumed, that the rope follows a linear extension. According to Hooke's law, the elastic extension is defined as

$$\Delta L = \frac{L \cdot F}{E \cdot A} \tag{C.1}$$

were, ΔL is the elastic extension of the line, L is the length of the line, F is the towing load, E is the modulus of elasticity and A is the cross-sectional area of the rope. The modulus of elasticity and the rope area were scaled individually by λ and λ^2 respectively – note that λ is the model's scaling factor 1:50. After scaling and rearranging, the result was a ratio of force over extension, which is the required spring constant of the towing line spring c, resembling the elasticity at model scale

$$c = \frac{F}{\Delta L} = \frac{E \cdot A}{L \cdot \lambda^2} \tag{C.2}$$

The spring constant c depends on the Cauchy number

$$Cy = \frac{\rho \cdot v^2}{E} \tag{C.2}$$

where, ρ is the density of the water in kg/m^3, v is the towing velocity in m/s and E is the modulus of elasticity of the rope in kg/ms^2, which for this research is 0.439.

The catenary of a line defines its ratio between force and horizontal length. The ratio varies, depending on the force, acting like a highly progressive spring. The force-length ratio depends on the rope length and the specific weight of the line. To ensure the correct behaviour of the model towing line, its elasticity was corrected by arranging the length of the towing line at the model – using 2λ instead of λ for the length – while to ensure that the correct catenary shape was maintained at the model line, the weight of the model towing line was modified following an iterative process. Table 5 shows the characteristic parameters of the towing line system at prototype and model scale. The comparison between the towing line characteristics in full scale and model scale (Figure 15) shows a good agreement. Furthermore, a bridle with a 60° angle was used to connect the towing line to the top of the two fore buoyancy tanks (0.12 m above the still water level). Finally, to simulate an aft tug, a constant

weight of 160 g (20 t bollard pull at full scale) was applied on the top of the tower buoyancy tank via a Dyneema® rope.

Table 5: Parameters of the towing system at model and prototype scale.

Parameter	Prototype scale	Model scale	Scaling
Length	900 m	9 m	2λ
Minimum Breaking Load	1315 kN	10.5 N	Λ^3
Specific Weight	8.1 kg/m	8.7 g/m	-
Spring Rate	194 N/mm	0.078 N/mm	Cauchy

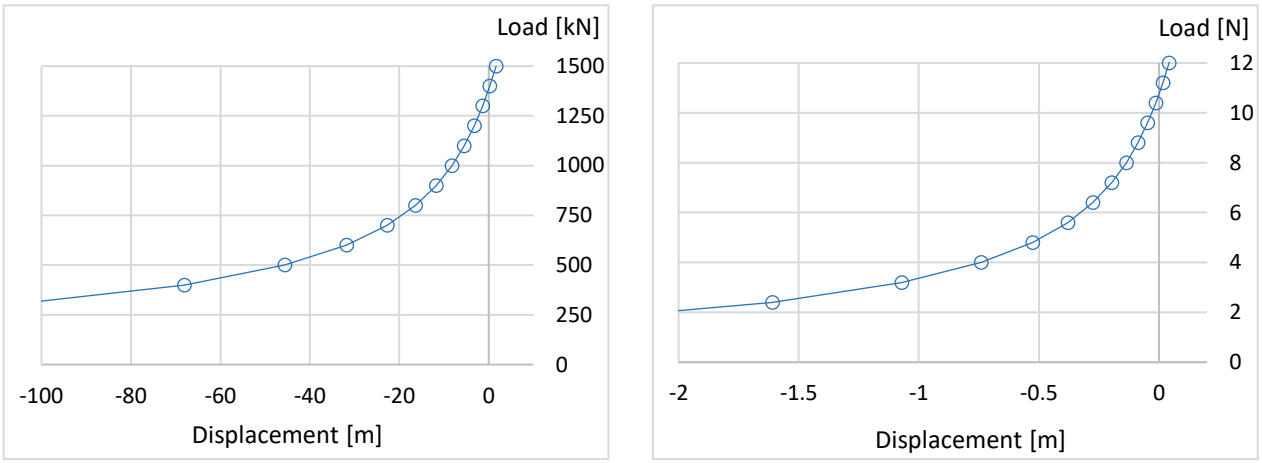

(a) (b)

Figure 15: Towing line characteristics at prototype scale (a) and model scale (b).

REFERENCES

Abanades, J., 2019. Wind Energy in the Mediterranean Spanish ARC: The Application of Gravity Based Solutions. Frontiers in Energy Research 7, 83. https://doi.org/10.3389/fenrg.2019.00083

Abanades, J., Ivars, J., Molina, R., García, C., 2018. The Application of Caisson-Type Solutions to the Current Offshore Wind Energy Market, in: OMAE2018. Volume 1: Offshore Technology. https://doi.org/10.1115/OMAE2018-77508

Adam, F., Großmann, J., Schuldt, B., 2016. Comparing Measured Results of Scaled Towing Tests of a Floating Substructure for Offshore Wind Turbines with Calculated Results.

Amante, J., Sánchez, G.D., González, G., 2016. Development of a Semi-submersible Barge for the installation of a TLP floating substructure. TLPWIND ® case study. Journal of Physics: Conference Series 749, 012016.

Baquerizo, A., Losada, M.A., Smith, J.M., 1998. Wave reflection from beaches: A predictive model. Journal of coastal research 291–298.

Barnes, I., Herring, R., Myers, E., Radevsky, O., Wincott, M., 2017. Design of an Offshore Floating Wind Energy Platform. University of Bristol.

Biran, A., Pulido, R.L., 2014. Ship hydrostatics and stability, 2nd ed. Butterworth-Heinemann, Oxford, UK.

Borg, M., Walkusch Jensen, M., Urquhart, S., Andersen, M.T., Thomsen, J.B., Stiesdal, H., 2020. Technical Definition of the TetraSpar Demonstrator Floating Wind Turbine Foundation. Energies 13. https://doi.org/10.3390/en13184911

Bredmose, H., Borg, M., Pegalajar-Jurado, A., Nielsen, T.R., Madsen, F.J., Lomholt, A.K., Mikkelsen, R., Mirzaei, M., 2017. TetraSpar Floating Wind Turbine Scale Model Testing Summary Report (No. Test Report 1). Stiesdal Offshore Technologies, DHI, and DTU Wind Energy, Kongens Lyngby, DK.

Bureau veritas, 2015. Classification and Certification of Floating Offshore Wind Turbines: NI/572/DT/R01/E.

Butterfield, S., Musial, W., Jonkman, J., Sclavounos, P.D., 2005. Engineering Challenges for Floating Offshore Wind Turbines. Presented at the in: proceedings of the 2005 Copenhagen Offshore Wind Conference.

Castro-Santos, L., Diaz-Casas, V., 2015. Economic influence of location in floating offshore wind farms. Ocean Engineering 107, 13–22. https://doi.org/10.1016/j.oceaneng.2015.07.025

Castro-Santos, L., Silva, D., Bento, A.R., Salvação, N., Guedes Soares, C., 2020. Economic feasibility of floating offshore wind farms in Portugal. Ocean Engineering 207, 107393. https://doi.org/10.1016/j.oceaneng.2020.107393

Chakrabarti, S.K., 1998. Physical model testing of floating offshore structures. Presented at the in: proceedings of the dynamic positioning conference, Citeseer.

Collins, K., Iglesias, G., Greaves, D., Toffoli, A., Stripling, S., 2015. The New Coast Laboratory at Plymouth University: A World-Class Facility for Marine Energy, in: From Sea to Shore – Meeting the Challenges of the Sea. pp. 1326–1335. https://doi.org/10.1680/fsts.59757.144

Collu, M., Maggi, A., Gualeni, P., Rizzo, C.M., Brennan, F.P., 2014. Stability requirements for floating offshore wind turbine (FOWT) during assembly and temporary phases: Overview and application. Ocean Engineering 84, 164–175. https://doi.org/10.1016/j.oceaneng.2014.03.018

Ding, H., Han, Y., Le, C., Zhang, P., 2017. Dynamic analysis of a floating wind turbine in wet tows based on multi-body dynamics. Journal of Renewable and Sustainable Energy 9, 033301. https://doi.org/10.1063/1.4982742

DNV GL, 2018a. Floating wind turbine structures: DNVGL-ST-0119.

DNV GL, 2018b. Marine operations and marine warranty: DNVGL-DT-N001.

El-Gabry, L.A., Thurman, D.R., Poisantte, P.E., 2014. Procedure for Determining Turbulence Length Scales Using Hotwire Anemometry (Technical Memorendum No. NASA/TM-2021-218403). NASA.

Equinor [WWW Document], 2019. URL https://www.equinor.com (accessed 8.1.19).

European Commission, 2021. COMMUNICATION FROM THE COMMISSION TO THE EUROPEAN PARLIAMENT, THE COUNCIL, THE EUROPEAN ECONOMIC AND SOCIAL COMMITTEE AND THE COMMITTEE OF THE REGIONS: "Fit for 55": delivering the EU's 2030 Climate Target on the way to climate neutrality, COM(2021) 550 final.

European Commission, 2020. COMMUNICATION FROM THE COMMISSION TO THE EUROPEAN PARLIAMENT, THE COUNCIL, THE EUROPEAN ECONOMIC AND SOCIAL COMMITTEE AND THE COMMITTEE OF THE REGIONS: An EU Strategy to harness the potential of offshore renewable energy for a climate neutral future, COM(2020) 741 final.

Fraile, D., Tardieu, P., 2018. Wind in power 2017: Annual combined onshore and offshore wind energy statistics. Wind Europe, Brussels, Belgium.

Fujiwara, T., Saito, M., Maeda, K., Sato, H., Ishida, K., 2013. Experimental Investigation of VIM Characteristics on Column Type Floater in Super Critical Reynolds Number V005T06A035. https://doi.org/10.1115/OMAE2013-10473

Hann, M., Perez-Collazo, C., 2018. Chapter 7: Physical Modelling, in: Greaves, D., Iglesias, G. (Eds.), Wave and Tidal Energy. John Wiley & Sons Ltd, West Sussex, UK, pp. 233–288.

Hyland, T., Adam, F., Dahlias, F., Großmann, J., 2014. Towing tests with the GICON®-TLP for Wind Turbines.

Ishihara, T., Zhang, S., 2019. Prediction of dynamic response of semi-submersible floating offshore wind turbine using augmented Morison's equation with frequency dependent hydrodynamic coefficients. Renewable Energy 131, 1186–1207. https://doi.org/10.1016/j.renene.2018.08.042

James, R., Costa Ros, M., 2015. Floating offshore wind: Market and technology review. The Carbon Trust, London, UK.

Jonkman, J., Butterfield, S., Musial, W., DScott, G., 2009. Definition of a 5-MW Reference Wind Turbine for Offshore System Development (No. NREL/TP-500-38060). National Renewable Energy Laboratory, Golden, CO, USA.

Lerch, M., De-Prada-Gil, M., Molins, C., Benveniste, G., 2018. Sensitivity analysis on the levelized cost of energy for floating offshore wind farms. Sustainable Energy Technologies and Assessments 30, 77–90. https://doi.org/10.1016/j.seta.2018.09.005

LIFES50+, 2021. LIFES50+ project website [WWW Document]. URL https://lifes50plus.eu/ (accessed 11.4.21).

Lopes, M.F.P., 2011. Experimental development of offshore wave energy converters (PhD). Instituto Superior Tecnico, Lisbon.

Mansard, E.P., Funke, E.R., 1980. The measurement of incident and reflected spectra using a least squares method. Presented at the In: Proceedings of the international conference on coastal engineering (ICCE).

Mueller, K., Faerron-Guzmán, R., Manjock, A., Borg, M., 2015. Lifes50plus deliverable: D.7.7 identification of critical environmental conditions and design load cases. Stuttgart.

Myhr, A., Bjerkseter, C., Ågotnes, A., Nygaard, T.A., 2014. Levelised cost of energy for offshore floating wind turbines in a life cycle perspective. Renewable Energy 66, 714–728. http://dx.doi.org/10.1016/j.renene.2014.01.017

Perez-Collazo, C., Pemberton, R., Greaves, D., Iglesias, G., 2019. Monopile-mounted wave energy converter for a hybrid wind-wave system. Energy Conversion and Management 199, 111971. https://doi.org/10.1016/j.enconman.2019.111971

Principle Power Inc, 2015. WindFloat web page [WWW Document].

Ramírez, L., Fraile, D., Brindley, G., 2021. Offshore Wind in Europe: Key trends and statistics 2020. Wind Europe, Brussels, Belgium.

Roddier, D., Cermelli, C., Aubault, A., Weinstein, A., 2010. WindFloat: A floating foundation for offshore wind turbines. Journal of renewable and sustainable energy 2, 033104–34.

Saitec [WWW Document], 2019. URL https://saitec-offshore.com/ (accessed 8.1.19).

Schuldt, B., 2006. Schwimmende Fundamentierung als Alternative für große Wassertiefen. Schiff & Hafen (Offshore Technik) 10, 6.

Tande, J.O.G., Merz, K., Paulsen, U.S., Svendsen, H.G., 2015. Floating offshore turbines. Wiley Interdisciplinary Reviews: Energy and Environment 4, 213–228. https://doi.org/10.1002/wene.130

Thomsen, J.B., Têtu, A., Stiesdal, H., 2021. A Comparative Investigation of Prevalent Hydrodynamic Modelling Approaches for Floating Offshore Wind Turbine Foundations: A TetraSpar Case Study. Journal of Marine Science and Engineering 9. https://doi.org/10.3390/jmse9070683

Turunen, J., Thambirajah, J., Larsson, M., Pal, B.C., Thornhill, N.F., Haarla, L.C., Hung, W.W., Carter, A.M., Rauhala, T., 2011. Comparison of Three Electromechanical Oscillation Damping Estimation Methods. IEEE Transactions on Power Systems 26, 2398–2407. https://doi.org/10.1109/TPWRS.2011.2155684

Villaespesa, E.B., Gonzalez, C.M., Martin, N.G.K., 2018. Transportation and Installation of a Floating Offshore Wind Turbine (Master). University of Aalborg, Aalborg, Denmark.

Wind Europe, 2021. It's official: The EU Commission wants 30 GW a year of new wind up to 2030 [WWW Document]. URL https://windeurope.org/newsroom/press-releases/its-official-the-eu-commission-wants-30-gw-of-new-wind-a-year-up-to-2030/ (accessed 10.5.21).

X1 Wind [WWW Document], 2019. URL http://www.x1wind.com (accessed 8.1.19).

Zuzzalova, M., 2017. Assessing the stability of the OrthoSpar offshore floating wind turbine based on the counterweight depth deployment (MSc). University of Plymouth, Plymouth, UK.